ADVANCING EARTH AND SPACE SCIENCES

Geophysical Research Letters

RESEARCH LETTER
10.1029/2023GL105761

Diagnosing the Sensitivity of Particulate Nitrate to Precursor Emissions Using Satellite Observations of Ammonia and Nitrogen Dioxide

Ruijun Dang[1], Daniel J. Jacob[1], Shixian Zhai[2], Pierre Coheur[3], Lieven Clarisse[3], Martin Van Damme[3,4], Drew C. Pendergrass[1], Jin-soo Choi[5], Jin-soo Park[5], Zirui Liu[6], and Hong Liao[7]

[1]John A. Paulson School of Engineering and Applied Sciences, Harvard University, Cambridge, MA, USA, [2]Earth System Science Programme, State Key Laboratory of Agrobiotechnology, Institute of Environment, Energy and Sustainability, The Chinese University of Hong Kong, Sha Tin, Hong Kong, [3]Université libre de Bruxelles (ULB), Spectroscopy, Quantum Chemistry and Atmospheric Remote Sensing (SQUARES), Brussels, Belgium, [4]Royal Belgian Institute for Space Aeronomy (BIRA-IASB), Brussels, Belgium, [5]Air Quality Research Division, National Institute of Environmental Research, Incheon, South Korea, [6]State Key Laboratory of Atmospheric Boundary Layer Physics and Atmospheric Chemistry, Institute of Atmospheric Physics, Chinese Academy of Sciences, Beijing, China, [7]Jiangsu Key Laboratory of Atmospheric Environment Monitoring and Pollution Control, Collaborative Innovation Center of Atmospheric Environment and Equipment Technology, School of Environmental Science and Engineering, Nanjing University of Information Science and Technology, Nanjing, China

Key Points:

- Reducing particulate nitrate pollution requires understanding its local sensitivities to NH_3, NO_x, and volatile organic compound emissions
- Satellite observation of the NH_3/NO_2 column ratio is an effective indicator for diagnosing these sensitivities
- IASI NH_3 and OMI NO_2 observations reveal varying regimes of nitrate sensitivity across wintertime East Asia

Supporting Information:

Supporting Information may be found in the online version of this article.

Correspondence to:

R. Dang,
rjdang@g.harvard.edu

Citation:

Dang, R., Jacob, D. J., Zhai, S., Coheur, P., Clarisse, L., Van Damme, M., et al. (2023). Diagnosing the sensitivity of particulate nitrate to precursor emissions using satellite observations of ammonia and nitrogen dioxide. *Geophysical Research Letters*, *50*, e2023GL105761. https://doi.org/10.1029/2023GL105761

Received 1 AUG 2023
Accepted 18 NOV 2023

Abstract Particulate nitrate is a major component of fine particulate matter ($PM_{2.5}$). Its formation may be varyingly sensitive to emissions of ammonia (NH_3), nitrogen oxides ($NO_x \equiv NO + NO_2$), and volatile organic compounds (VOCs), depending on local conditions. Diagnosing these sensitivities is critical for successful air quality management. Here, we show that satellite measurements of tropospheric NH_3 and NO_2 columns can be used as a quick indicator of the dominant sensitivity regime through the NH_3/NO_2 column ratio together with the NO_2 column. We demonstrate the effectiveness of this indicator with the GEOS-Chem chemical transport model and define thresholds to separate the different sensitivity regimes. Applying the method to wintertime IASI and OMI observations in East Asia reveals that surface nitrate is dominantly VOC-sensitive in the southern North China Plain (NCP), NO_x-sensitive in most of the East China Plain, and NH_3-sensitive in the northern NCP, southern China, and Korea.

Plain Language Summary We present a novel application of satellite remote sensing to better understand the causes of particulate nitrate pollution. Particulate nitrate is a major air pollutant throughout the urbanized world. It is produced by atmospheric oxidation of emitted nitrogen oxides (NO_x) but may be more sensitive to emissions of ammonia (NH_3) or volatile organic compounds (VOCs). Understanding which of NH_3, NO_x, or VOC emissions is most important in driving nitrate formation is critical for air quality management. We show that satellite measurements of the NH_3/NO_2 column ratio along with NO_2 columns is an effective indicator to determine the dominant sensitivity regime (NH_3-, NO_x-, or VOC − sensitive). We develop this approach using an atmospheric chemistry model and apply it to wintertime satellite observations in East Asia. The approach should be applicable to other continents, seasons, and a broader range of satellite instruments, providing valuable insights for particulate nitrate reduction strategies.

1. Introduction

Particulate nitrate (pNO_3^-) is a major component of fine particulate matter ($PM_{2.5}$) throughout the urbanized world and particularly in winter. It drives $PM_{2.5}$ pollution events in East Asia (Li et al., 2018; H. Kim et al., 2020; Kim et al., 2022; Tian et al., 2019; Q. Xu et al., 2019), North America (Franchin et al., 2018; Womack et al., 2019), and Europe (Bressi et al., 2021). It is becoming relatively more important as other $PM_{2.5}$ components have decreased in response to emission controls (Attwood et al., 2014; Zhai et al., 2019), but pNO_3^- has not (Leung et al., 2020; Li et al., 2019; Zhai et al., 2023; Zhou et al., 2022). In eastern China, wintertime pNO_3^- concentrations have been flat over the past decade despite a 30% decrease in NO_x emissions (Chuang et al., 2021; Fu et al., 2020; Zhai et al., 2021). pNO_3^- has become a key target for further improving $PM_{2.5}$ air quality.

pNO_3^- is produced by the oxidation of nitrogen oxide radicals ($NO_x \equiv NO + NO_2$) to nitric acid (HNO_3). HNO_3 partitions into the aerosol as pNO_3^- depending on aerosol pH, water content, and temperature (Guo et al., 2018; Nenes et al., 2020). The presence of alkalinity, mostly from ammonia (NH_3), raises aerosol pH to favor pNO_3^- formation. The resulting pNO_3^- is mainly in the fine $PM_{2.5}$ aerosol mode. NO_x in urban areas mainly comes from fuel combustion. NH_3 originates from agricultural activities including fertilizer use and livestock manure, but vehicle emissions could also be important in urban areas (Farren et al., 2020; Y. Wang et al., 2023). Oxidation of NO_x to HNO_3 is by the hydroxyl radical (OH) during the daytime and by ozone (O_3) at night, both of which depend on the levels of NO_x and volatile organic compounds (VOCs). VOCs originate from combustion, industrial and domestic chemical products, vegetation, and open fires (Shen et al., 2019).

pNO_3^- concentrations are generally highest in winter when low temperatures favor partitioning into the aerosol. Formation of pNO_3^- may then be dominantly sensitive to the gas in shortest supply, either NH_3 or HNO_3 (Nenes et al., 2020), while the NO_x to HNO_3 conversion is limited by either the abundance of NO_x or VOCs (Kleinman, 1994; Womack et al., 2019). Other factors can further complicate these relationships of pNO_3^- to emitted precursors, including competing deposition between HNO_3 and pNO_3^- (Zhai et al., 2021), other sources of aerosol alkalinity (Guo et al., 2018), and NO_x oxidation to organic nitrates (Romer Present et al., 2020). Coarse pNO_3^- can also form from uptake of HNO_3 by alkaline soil dust and sea salt in dusty and coastal areas (Zhai et al., 2023). The sensitivity of pNO_3^- concentrations to NH_3, NO_x, and VOC emissions is thus nonlinear and complex, requiring different control strategies under different conditions.

Two approaches have been used to determine the sensitivity of pNO_3^- to emissions. Field studies measure aerosols and gases, allowing for the calculation of diagnostic indicators (Petetin et al., 2016; Z. Xu et al., 2019), or providing input to thermodynamic models for sensitivity tests (Franchin et al., 2018; Guo et al., 2018). They require substantial experimental resources, and the results are only locally applicable. Chemical transport models diagnose the sensitivity of pNO_3^- to emissions through simulations with perturbed emissions (Fu et al., 2020; Li et al., 2021; Zhai et al., 2021). They require substantial computational resources, and emission errors in the model may lead to misdiagnosis.

Here we present a new satellite-based method to diagnose locally the sensitivities of fine pNO_3^- formation to NH_3, NO_x, and VOC emissions. We use for this purpose satellite measurements of the tropospheric column concentrations of NH_3 (Ω_{NH3}) and NO_2 (Ω_{NO2}) and diagnose the sensitivity from the $\Omega_{NH3}/\Omega_{NO2}$ ratio. Our approach parallels the common use of the space-based formaldehyde $HCHO/NO_2$ column ratio as an indicator for whether O_3 formation is NO_x- or VOC-limited (Duncan et al., 2010; Jin et al., 2020; Martin et al., 2004). It offers a quick diagnostic tool for air quality management in their design of pNO_3^- control strategies. NH_3 measurements from space have been available from the IASI instrument since 2007 (Clarisse et al., 2009), and from the CrIS instrument since 2012 (Shephard and Cady-Pereira, 2015). NO_2 measurements from space began with the GOME instrument in 1995 (Martin et al., 2002) and have continued with the OMI instrument since 2005 (Lamsal et al., 2021), the TROPOMI instrument since 2017 (van Geffen et al., 2020), and the GEMS geostationary instrument since 2020 (J. Kim et al., 2020). We demonstrate the method for East Asia in winter, using observations from OMI and IASI.

2. Theoretical Basis: Ω_{NH3} and Ω_{NO2} as Indicators of Nitrate Formation Regime

The main pathway for fine pNO_3^- formation is the joint condensation of NH_3 and HNO_3, governed by a thermodynamic equilibrium constant K dependent on temperature and relative humidity (RH) (Stelson and Seinfeld, 1982):

$$K = p_{NH_3} \times p_{HNO_3}, \tag{1}$$

where p is partial pressure. At low wintertime temperatures and/or high RH, the low value of K leads to titration where pNO_3^- formation is mainly sensitive to the gas in shortest supply, either NH_3 or HNO_3. At warmer temperatures, NH_3 and HNO_3 may coexist in the gas phase but the dominant sensitivity is still to the gas in shortest supply (Nenes et al., 2020). Scavenging of NH_3 by acid sulfate may totally suppress pNO_3^- formation when sulfate is in excess of NH_3 (Ansari and Pandis, 1998). Dust and sea salt particles can also drive HNO_3 into the aerosol through added alkalinity or chloride displacement (Alexander et al., 2005; Fairlie et al., 2010), though this tends to be in coarser particles than $PM_{2.5}$. Henceforth we will refer to pNO_3^- as the fine $PM_{2.5}$ component of nitrate.

Several frameworks exist for determining the dominant sensitivities in thermodynamic formation of pNO_3^-. Nenes et al. (2020) pointed out that aerosol pH is the key variable affecting the dominant pNO_3^- sensitivity to NH_3 or HNO_3, and the pH thresholds for distinguishing between the regimes depend on temperature and aerosol

liquid water content. In a more simplified framework, the molar ratio R of free ammonia after sulfate neutralization ($NH_3 + NH_4^+ - 2 \times SO_4^{2-}$) to total nitrate ($NO_3^T \equiv HNO_3 + pNO_3^-$) is measured in field campaigns to diagnose the sensitivities (Petetin et al., 2016; Z. Xu et al., 2019). The effect of pH is implicitly considered within this simplified indicator through the role of NH_3 (Guo et al., 2017, 2018). Generally, $R > 1$ indicates dominant sensitivity to HNO_3, while $R < 1$ indicates dominant sensitivity to NH_3. The gas-phase NH_3/HNO_3 ratio can also serve as an indicator but its threshold for transition between regimes may depart from unity when NO_3^T is heavily partitioned into the aerosol and the resulting HNO_3 concentration is very low. A dominant sensitivity to HNO_3 would be expected to translate into a dominant sensitivity to NO_x emissions, but the conversion of NO_x to HNO_3 may in fact be limited by the supply of VOCs under VOC-limited conditions for oxidant (OH and O_3) formation. Womack et al. (2019) point out that this may cause pNO_3^- formation to be most sensitive to VOC emissions under strongly VOC-limited conditions as frequently occur in urban environments in winter.

Satellites measure tropospheric columns of NH_3 (Ω_{NH3}) and NO_2 (Ω_{NO2}). It follows from the above discussion that the measured $\Omega_{NH3}/\Omega_{NO2}$ ratio should give an indicator of the sensitivity of pNO_3^- formation to precursor emissions, in a manner useful to air quality management. Application of this indicator may be complicated by the vertical gradients of NH_3 and NO_2 concentrations, by the presence of sulfate, and by the limiting regime for oxidation of NO_x to HNO_3. A model analysis can evaluate these complications, and this is discussed in the next section. Satellite observations of HCHO columns (Ω_{HCHO}) could in principle distinguish between NO_x- and VOC-limited oxidant regimes through consideration of the $\Omega_{HCHO}/\Omega_{NO2}$ ratio, but in practice wintertime Ω_{HCHO} concentrations are near or below the detection limit (Zhu et al., 2014, 2017). Very high Ω_{NO2} values can be used instead as an indicator of VOC-limited conditions (Sillman, 1995).

3. Evaluation in the GEOS-Chem Model Environment

To analyze the value of the $\Omega_{NH3}/\Omega_{NO2}$ ratio as an indicator for the sensitivity of pNO_3^- formation to emissions, we conduct sensitivity simulations with the GEOS-Chem global atmospheric chemistry model. We use GEOS-Chem version 13.4.1 (DOI: https://zenodo.org/record/6564702) with options and modifications described below. The simulations are driven by MERRA-2 meteorology and are conducted at a nested resolution of 0.5° × 0.625° for East Asia (90°–145°E, 10°–55°N) over the 1–31 January 2017 period, with boundary conditions updated every 3 hr from a 4° × 5° global simulation. The simulation is spun up for 6 months for initialization.

GEOS-Chem includes detailed oxidant-aerosol chemistry (Wang et al., 2021). Thermodynamic pNO_3^- formation from NH_3–HNO_3–H_2SO_4–HCl mixtures is calculated by ISORROPIA II (Fountoukis and Nenes, 2007) and defines in the model the $PM_{2.5}$ component of pNO_3^-. The model also includes uptake of HNO_3 by coarse sea salt aerosol (Wang et al., 2021) but this does not contribute to $PM_{2.5}$ and is not considered here in pNO_3^- accounting. Uptake of HNO_3 by dust is included in GEOS-Chem as an option (Fairlie et al., 2010; Zhai et al., 2023) but is not used in our simulation. We use the wet deposition scheme of Luo et al. (2020), which is an option in GEOS-Chem and has proven to be important for successful simulation of pNO_3^- (Luo et al., 2019, 2020; Zhai et al., 2021). We also add to our simulation the photolysis of aerosol nitrate, which improves the simulation of tropospheric NO_2 column observations in GEOS-Chem though the effect is small in winter (Dang, Jacob, Shah, et al., 2023; Shah et al., 2023). Global anthropogenic emissions are from the Community Emissions Data System (CEDS) (McDuffie et al., 2020) superseded by the MEIC inventory for China (Zheng et al., 2018) and the KORUSv5 inventory for South Korea. Other emissions settings are as described in Dang, Jacob, Shah, et al. (2023).

Figure 1 compares simulated pNO_3^- concentrations from our simulation with measurements from observational networks and field studies in China and Korea in winter 2016–2017. Table S1 in Supporting Information S1 gives site details. Most observations are centered on January 2017, but some are for December 2016, and some are for the whole winter (DJF). All are compared to GEOS-Chem in January 2017. GEOS-Chem simulates the ensemble observations with a correlation coefficient $r = 0.82$, a reduced-major-axis (RMA) regression slope of 0.98 ± 0.15, and a normalized mean bias (NMB) of 9%. There is one site in Xi'an where observed pNO_3^- is anomalously high (averaging 36 μg m^{-3}) and this is not captured by the model. This site is excluded from the statistics above. Additionally, GEOS-Chem has been found to reproduce daily pNO_3^- observations well at a Beijing site during the winters of 2014–2019 (Zhai et al., 2021). Overall, the successful simulation of pNO_3^- variability provides support for using the model to study the sensitivity of pNO_3^- to precursor emissions in East Asia.

We diagnose the local pNO_3^- sensitivity to NH_3, NO_x, and VOC emissions in the model by conducting sensitivity simulations with individual emissions reduced by 20%. The reduction is applied to all sources (anthropogenic

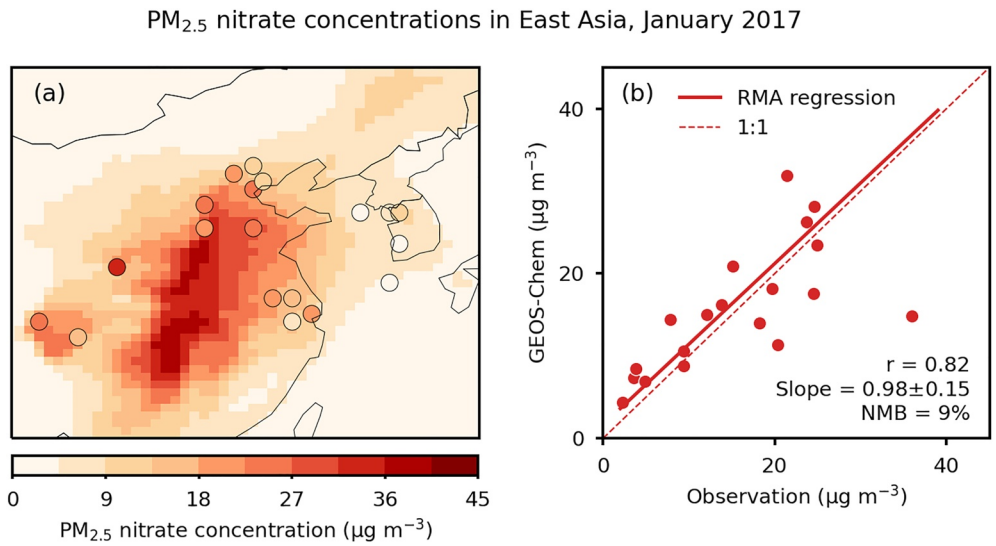

Figure 1. Surface $PM_{2.5}$ nitrate concentrations in China and Korea. Mean GEOS-Chem model concentrations for January 2017 are compared to mean observations at a number of sites (Table S1 in Supporting Information S1) over December-February 2017. Panel (a) shows the spatial distribution, with observations as circles and GEOS-Chem as solid contours. Panel (b) shows the correlation between model and observations at individual sites including correlation coefficient (r), normalized mean bias (NMB), reduced-major-axis (RMA) regression line and slope (±95% confidence interval), and 1:1 dashed line. The statistics excludes the Xi'an site where observed pNO_3^- is anomalously high. Site details are in Table S1 in Supporting Information S1.

and natural) but the sources in winter are mainly anthropogenic. The local model sensitivity S_i of pNO_3^- to the emission E_i of species i for individual 0.5° × 0.625° grid cells is calculated from the relative model differences (Δ) between the sensitivity and base simulations as:

$$S_i = \frac{\Delta \log\left[pNO_3^-\right]}{\Delta \log\ E_i}, \tag{2}$$

where i refers to NH_3, NO_x, or VOC, and $[pNO_3^-]$ refers to monthly mean concentrations in surface air. A sensitivity $S_i = 1$ indicates that a 20% reduction in emissions of precursor i results in a corresponding 20% decrease in surface pNO_3^- concentrations. By comparing S_{NH3}, S_{NOx}, and $S_{VOC,}$ we determine whether pNO_3^- in a model grid cell is most NH_3−, NO_x-, or VOC-sensitive.

Figure 2 shows the model relationship between the dominant pNO_3^- sensitivity and the observable surface and satellite indicators discussed in Section 2. Individual circles show the dominant sensitivities S_i for monthly mean surface pNO_3^- concentrations in individual grid cells. We use the NH_3/HNO_3 gas-phase molar ratio as surface indicator instead of R because it is better connected to the $\Omega_{NH3}/\Omega_{NO2}$ satellite indicator. We use NO_2 concentration (surface or column) as an indicator of VOC-limited conditions for NO_x oxidation because Ω_{HCHO} is generally not observable from space in winter. Surface indicators are 24-hr averages, while columns are sampled at 9–10 local time (LT) for NH_3 to emulate IASI and at 13–14 LT for NO_2 to emulate OMI. Averaging kernels are applied to the model NO_2 vertical profiles following Cooper et al. (2020) to emulate tropospheric NO_2 columns from version 4 of the NASA OMI NO_2 level 2 product (OMNO2) (Lamsal et al., 2021). We restrict our attention to grid cells with $\Omega_{NO2} > 2.5 \times 10^{15}$ molec cm^{-2} to remove remote regions (as shown by the satellite observations in Figure 3b) where diagnosing sensitivity to local emissions would be inappropriate.

Results in Figure 2 show that the indicators are successful at diagnosing the dominant pNO_3^- sensitivities to precursor emissions. Approximately 90% of the grid cells show a dominant sensitivity S_i that is distinctly greater than the other two sensitivities ($S_i/S_j > 1.1$). Black dashed lines delineate the transitions between sensitivity regimes. The slanted lines are derived from reduced-major-axis (RMA) linear regressions for grid cells with sensitivity ratios $0.95 < S_i/S_j < 1.05$. Sensitivities S_{NH3} and S_{NOx} can approach unity within the corresponding regimes. S_{VOC} can reach 0.5 in the VOC-sensitive regime.

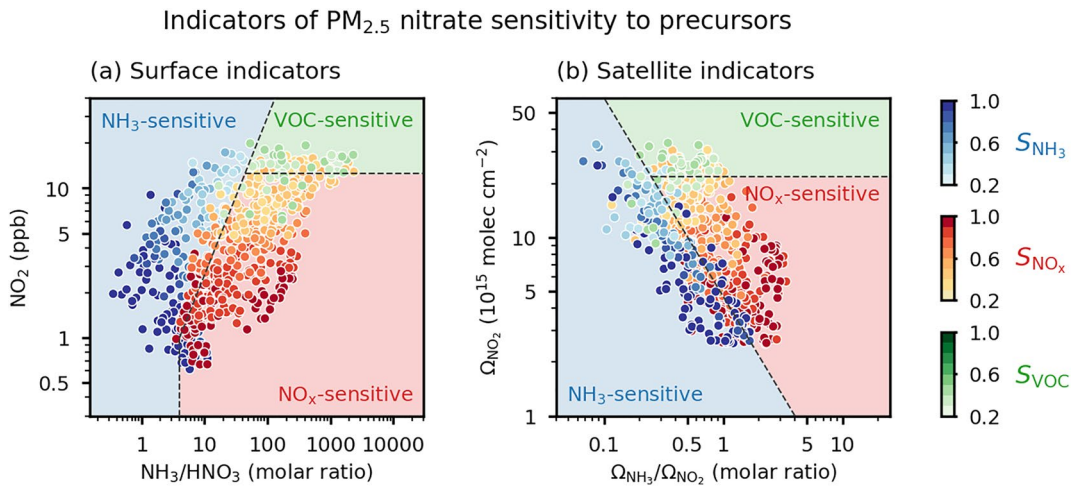

Figure 2. Regimes for the sensitivity of surface pNO_3^- concentrations to NH_3, NO_x, and VOC emissions. Results show the dominant sensitivities $S_i = \Delta\log[pNO_3^-]/\Delta\log E_i$ for monthly mean concentrations in January 2017 in individual $0.5° \times 0.625°$ GEOS-Chem model grid cells in East Asia (domain of Figure 1(a)). A sensitivity $S_i = 1$ indicates proportional response of the pNO_3^- concentration to change in the precursor emission E_i. The dominant sensitivities are plotted in a state space of indicators of the sensitivity regime as observable from surface or satellite measurements. Surface indicators (panel (a)) are the gas-phase NH_3/HNO_3 molar ratio and the NO_2 concentration. Satellite indicators (panel (b)) are the $\Omega_{NH3}/\Omega_{NO2}$ column ratio and the Ω_{NO2} column. Ω_{NH3} is sampled at 9–10 local time (LT) to emulate the IASI instrument, and Ω_{NO2} is sampled at 13–14 LT to emulate the OMI instrument. Dashed lines separate the different regimes as diagnosed by S_i. The slanted lines are derived from reduced-major-axis (RMA) linear regression for grid cells with sensitivity ratios $0.95 < S_i/S_j < 1.05$. The corresponding equations are given in the text. Ocean and remote grid cells with $\Omega_{NO2} < 2.5 \times 10^{15}$ molec cm^{-2} (see Figure 3b) are excluded from the plot.

Examining first the surface indicators, we find that NH_3-sensitive conditions are associated with $NH_3/HNO_3 < 4$ mol mol^{-1} at low NO_2, with the threshold increasing at higher NO_2. The threshold is larger than the value of 1 for the R ratio in Section 2. This is expected because the gas-phase HNO_3 concentration can be extremely low in winter, so that competing deposition between gas-phase HNO_3 and pNO_3^- increases sensitivity to NH_3 even when $R > 1$ (Zhai et al., 2021). Outside of the NH_3-sensitive regime, whether NO_x or VOCs is the controlling precursor is well delineated by NO_2 levels. For $NO_2 < 12$ ppb the sensitivity is mostly to NO_x emissions (NO_x-limited regime) but it decreases as NO_2 increases and VOCs then become more important. For $NO_2 > 12$ ppb the sensitivity is mostly to VOCs (strongly VOC-limited regime). NH_3 sensitivity can also be dominant under these conditions because the conversion efficiency of NO_x to HNO_3 is low. The sensitivity regimes separated by the black dashed lines in Figure 2a are thus diagnosed from the gas-phase NH_3/HNO_3 and NO_2 surface indicator concentrations as

$$\mathrm{NH_3-sensitive:}\begin{cases}\dfrac{[NH_3]}{[HNO_3]} < 4 & ([NO_2] < 1.3\,\mathrm{ppb})\\ \log\dfrac{[NH_3]}{[HNO_3]} < 0.49 + 1.02\times\log[NO_2] & ([NO_2] > 1.3\,\mathrm{ppb})\end{cases}, \tag{3a}$$

$$\mathrm{NO_x-sensitive:}\begin{cases}\dfrac{[NH_3]}{[HNO_3]} > 4 & ([NO_2] < 1.3\,\mathrm{ppb})\\ \log\dfrac{[NH_3]}{[HNO_3]} > 0.49 + 1.02\times\log[NO_2] & (1.3\,\mathrm{ppb} < [NO_2] < 12\,\mathrm{ppb})\end{cases}, \tag{3b}$$

$$\mathrm{VOC-sensitive:}\ \log\frac{[NH_3]}{[HNO_3]} > 0.49 + 1.02\times\log[NO_2] \qquad ([NO_2] > 12\mathrm{ppb}). \tag{3c}$$

Figure 2b shows that the satellite indicators are similarly effective for diagnosing sensitivity regimes. For a given $\Omega_{NH3}/\Omega_{NO2}$ ratio, higher Ω_{NO2} levels indicate a lower efficiency in converting NO_2 to HNO_3, so that NH_3

is more likely to be in excess. This explains why the threshold $\Omega_{NH3}/\Omega_{NO2}$ ratio for transition from NH_3-sensitive to NO_x-sensitive conditions decreases with increasing Ω_{NO2}, while by contrast the threshold NH_3/HNO_3 ratio in surface observations increases with increasing NO_2. We also see from Figure 2 that Ω_{NO2} can serve as a good satellite indicator for the onset of VOC-sensitive conditions. The sensitivity regimes separated by the black dashed lines in Figure 2b are thus diagnosed from the Ω_{NH3} and Ω_{NO2} columns as

$$\mathrm{NH_3-sensitive:}\ \log\frac{\Omega_{NH_3}}{\Omega_{NO_2}} < 14.09 - 0.90\times\log\Omega_{NO_2}, \tag{4a}$$

$$\mathrm{NO_x-sensitive:}\ \log\frac{\Omega_{NH_3}}{\Omega_{NO_2}} > 14.09 - 0.90\times\log\Omega_{NO_2}\left(\Omega_{NO_2} < 2\times10^{16}\mathrm{molec\,cm^{-2}}\right), \tag{4b}$$

$$\mathrm{VOC-sensitive:}\ \log\frac{\Omega_{NH_3}}{\Omega_{NO_2}} > 14.09 - 0.90\times\log\Omega_{NO_2}\left(\Omega_{NO_2} > 2\times10^{16}\mathrm{molec\,cm^{-2}}\right). \tag{4c}$$

4. Application to Satellite Observations

We now illustrate the application of the method to satellite observations of Ω_{NH3} from IASI and Ω_{NO2} from OMI, using Equation 4 to diagnose the sensitivity regimes in the observations. The IASI instrument measures Ω_{NH3} by observing the infrared radiation emitted by the Earth's surface and the atmosphere. It provides global coverage twice a day, at 9:30 local solar time (LT) and 21:30 LT, with a nadir pixel resolution of 12×12 km^2 (Van Damme et al., 2014). The OMI instrument measures Ω_{NO2} by observing solar backscatter, providing daily global coverage at 13:30 LT with a nadir pixel resolution of 13×24 km^2. Here, we use version 3 of the reanalyzed level 2 product of NH_3 columns (ANNI-NH_3-v3R) (Van Damme et al., 2021) and version 4 of the NASA OMI NO_2 level 2 product (OMNO2) (Lamsal et al., 2021) during the winter (DJF) of 2017. Both products have been extensively validated including for IASI v3 (Guo et al., 2021; Vohra et al., 2021; Wang et al., 2022; R. Wang et al., 2023) and OMNO2 version 4 (Lamsal et al., 2021). Both data sets have been used effectively in previous studies for hotspot detection (Clarisse et al., 2019; Mebust et al., 2011) and emission tracking (Chen et al., 2021; Cooper et al., 2022; Evangeliou et al., 2021; Luo et al., 2022; Marais et al., 2021; Shah et al., 2020).

We only use morning overpasses (9:30 LT) for Ω_{NH3} to minimize the time separation with OMI afternoon observations. We filter the IASI Ω_{NH3} data to remove pixels with cloud fraction >0.1. For OMI Ω_{NO2} data, we filter out pixels with cloud fraction >0.3, surface reflectivity >0.3, solar zenith angle >75°, viewing zenith angle >65°, and those affected by the so-called row anomaly. To reduce noise, both data sets are gridded and averaged to obtain wintertime mean columns at $0.5°\times0.625°$ resolution, and grid cells with fewer than 30 successful retrievals for either Ω_{NH3} or Ω_{NO2} are excluded. Additional filtering is applied to the gridded wintertime means to remove negative values. Uncertainties in grid-cell averages for both data sets are calculated using the method described by Eskes et al. (2003), with a 0.15 error correlation applied to retrievals falling within the same grid cell (Boersma et al., 2018). The calculated uncertainties range from 14% to 85% (0.1–0.9 quantiles) for IASI Ω_{NH3} and 9% to 26% for OMI Ω_{NO2} over the studied region (Figure 3) during the winter of 2017.

Figures 3a and 3b show the IASI Ω_{NH3} and OMI Ω_{NO2} during the winter of 2017. IASI observes high NH_3 in the East China Plain where it originates from livestock waste, fertilizer use, and vehicles (Zhang et al., 2018). OMI observes high NO_2 in the densely populated East China Plain and the Seoul metropolitan area (SMA) in South Korea. These satellite observations of Ω_{NH3} and Ω_{NO2} are roughly consistent with the GEOS-Chem simulations (Figures S1 and S2 in Supporting Information S1) but that is not a requirement for application of our method.

Figure 3d shows the dominant local surface pNO_3^- sensitivities to precursor emissions determined from the observed $\Omega_{NH3}/\Omega_{NO2}$ ratio (Figure 3c) and Ω_{NO2} (Figure 3b) by applying Equation 4. We assume that the thresholds obtained from Equation 4 in January can represent the entirety of winter (DJF), considering that the effect of meteorological variability over those 3 months is small compared to the range of conditions within the spatial domain sampled by the model. Robustness tests are conducted for each grid cell by applying 10,000 Monte Carlo samplings for both IASI Ω_{NH3} and OMI Ω_{NO2} data, with grid means and uncertainties as inputs to describe the distributions. Grid cells exhibiting a robust diagnosis with a 90% confidence level are marked with black dots.

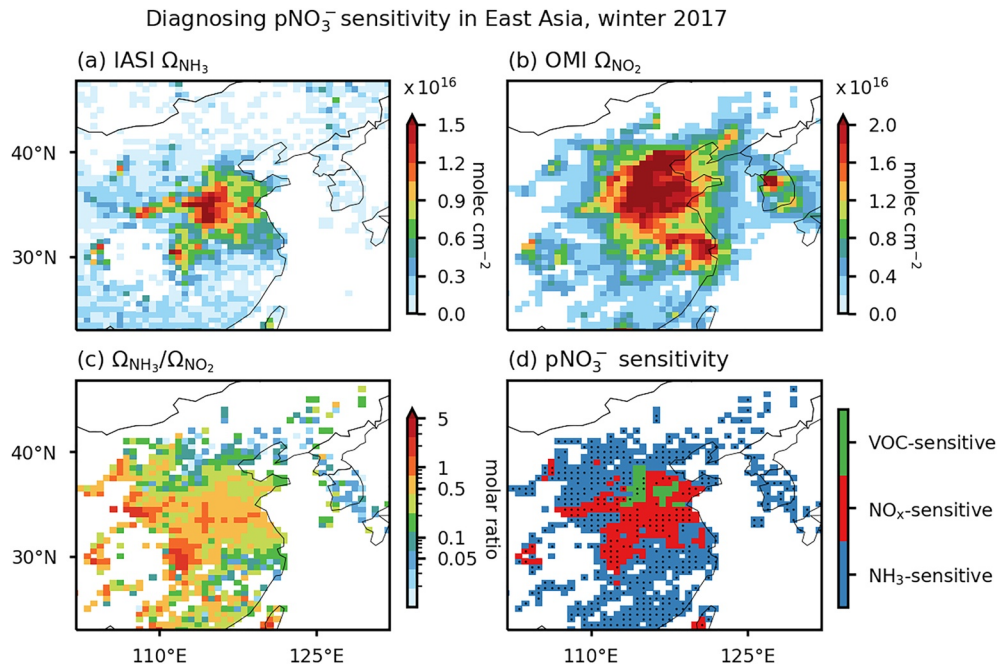

Figure 3. Sensitivity of surface particulate nitrate (pNO_3^-) concentrations in East Asia to precursor emissions as diagnosed from mean satellite observations in winter (DJF) 2016–2017. Panels (a) and (b) show IASI observations of NH_3 columns (Ω_{NH3}) and OMI observations of tropospheric NO_2 columns (Ω_{NO2}), filtered as described in the text. Panel (c) shows the molar $\Omega_{NH3}/\Omega_{NO2}$ ratio computed from the seasonal mean columns. Panel (d) presents the dominant sensitivity regimes of pNO_3^- diagnosed from the satellite observations using Equation 4. White areas indicate either lack of data or remote areas ($\Omega_{NO2} < 2.5 \times 10^{15}$ molec cm^{-2}). Black dots indicate grid cells with robust diagnoses at a 90% confidence level, determined through 10,000 Monte Carlo samplings for both Ω_{NH3} and Ω_{NO2}.

We find varying regimes of pNO_3^- sensitivity across China and Korea. VOC-sensitive conditions are observed in the southern North China Plain (NCP), characterized by a $\Omega_{NH3}/\Omega_{NO2}$ molar ratio exceeding 0.5 and Ω_{NO2} exceeding 2×10^{16} molec cm^{-2}. In this region, pNO_3^- formation is NH_3-saturated, and the most effective approach to decrease pNO_3^- is to control VOC emissions. In other areas of the East China Plain including Henan and Hubei provinces, and in the Fenwei Plain, the satellite observations indicate NO_x-sensitive conditions. In these areas, NH_3 levels are high and NO_x concentrations are not as high as in the southern NCP, so controlling NO_x emissions is the most effective way for decreasing pNO_3^-. NH_3-sensitive conditions are observed in the northern NCP (including Beijing), southern China, and Korea, characterized by relatively low $\Omega_{NH3}/\Omega_{NO2}$ ratios.

Previous field studies found that pNO_3^- formation at sites in eastern China are more sensitive to total nitrate than to NH_3 due to NH_3 being present in excess (Guo et al., 2018; Lin et al., 2020; Song et al., 2019; Zang et al., 2022). However, difference in the lifetimes of HNO_3 and pNO_3^- against deposition can drive a dominant sensitivity to NH_3 even when NH_3 is present in excess (Nenes et al., 2021; Zhai et al., 2021), as reflected in our GEOS-Chem simulation where the NH_3-sensitive regime extends to NH_3/HNO_3 gas-phase ratios in excess of unity (Figure 2a). Our findings are consistent with previous model studies, where wintertime pNO_3^- concentrations are found to be most sensitive to NH_3 and/or VOC controls in the NCP (Fu et al., 2020; Li et al., 2021; Zhai et al., 2021) and to NH_3 controls in the Yangtze River Delta (Li et al., 2021) and southern China (Lu et al., 2021).

Our demonstration of this satellite-based method for diagnosing the sensitivity of pNO_3^- to emissions has focused on wintertime East Asia, where pNO_3^- is particularly high. One might expect the same method and similar thresholds to be applicable to other polluted regions and seasons, but this would need to be further investigated with model simulations and evaluated with local field studies.

In summary, we have shown that NH_3 and NO_2 measurements from space can be used as a NH_3/NO_2 column ratio indicator to diagnose the sensitivity of $PM_{2.5}$ nitrate to emissions in support of pollution management. Our method could be applied to other current satellite instruments including TROPOMI for NO_2 and CrIS for NH_3. Future geostationary satellites including Sentinel-4 and IRS for Europe (Gulde et al., 2017) and GeoXO for the

United States (Schmit et al., 2022) will have NO_2 and NH_3 measurements from the same platform. The Nitrosat satellite mission presently under consideration by the European Space Agency will simultaneously observe NH_3 and NO_2 at 500-m resolution, greatly increasing the frequency of clear-sky scenes (Coheur et al., 2021). There is thus considerable potential for application of our method to the next generation of satellite observations. This new satellite-based method would enable us to gain a global perspective on pNO_3^- sensitivity and monitor regime changes.

Data Availability Statement

The IASI reanalyzed daily NH_3 data are publicly available from Clarisse et al. (2022). The OMNO2 product, created by the National Aeronautics and Space Administration (NASA), is available at Krotkov et al. (2019). The $PM_{2.5}$ nitrate observation data that are collected in this study can be accessed via Dang, Jacob, Zhai, et al. (2023).

Acknowledgments
This work was funded by the Harvard–NUIST Joint Laboratory for Air Quality and Climate and the Samsung $PM_{2.5}$ Strategic Research Program. The research in Belgium was supported by the Belgian Science Policy Office (BELSPO, Prodex HIRS and FED-tWIN ARENBERG projects) and the Air Liquide Foundation (TAPIR project). L. Clarisse is Research Associate supported by the Belgian F.R.S.-FNRS.

References

Alexander, B., Park, R. J., Jacob, D. J., Li, Q. B., Yantosca, R. M., Savarino, J., et al. (2005). Sulfate formation in sea-salt aerosols: Constraints from oxygen isotopes. *Journal of Geophysical Research*, *110*(D10), D10307. https://doi.org/10.1029/2004JD005659

Ansari, A. S., & Pandis, S. N. (1998). Response of inorganic PM to precursor concentrations. *Environmental Science and Technology*, *32*(18), 2706–2714. https://doi.org/10.1021/es971130j

Attwood, A. R., Washenfelder, R. A., Brock, C. A., Hu, W., Baumann, K., Campuzano-Jost, P., et al. (2014). Trends in sulfate and organic aerosol mass in the Southeast U.S.: Impact on aerosol optical depth and radiative forcing. *Geophysical Research Letters*, *41*(21), 7701–7709. https://doi.org/10.1002/2014GL061669

Boersma, K. F., Eskes, H. J., Richter, A., De Smedt, I., Lorente, A., Beirle, S., et al. (2018). Improving algorithms and uncertainty estimates for satellite NO_2 retrievals: Results from the quality assurance for the essential climate variables (QA4ECV) project. *Atmospheric Measurement Techniques*, *11*(12), 6651–6678. https://doi.org/10.5194/amt-11-6651-2018

Bressi, M., Cavalli, F., Putaud, J. P., Fröhlich, R., Petit, J. E., Aas, W., et al. (2021). A European aerosol phenomenology - 7: High-time resolution chemical characteristics of submicron particulate matter across Europe. *Atmospheric Environment: X*, *10*, 100108. https://doi.org/10.1016/j.aeaoa.2021.100108

Chen, Y., Shen, H., Kaiser, J., Hu, Y., Capps, S. L., Zhao, S., et al. (2021). High-resolution hybrid inversion of IASI ammonia columns to constrain US ammonia emissions using the CMAQ adjoint model. *Atmospheric Chemistry and Physics*, *21*(3), 2067–2082. https://doi.org/10.5194/acp-21-2067-2021

Chuang, M.-T., Chou, C. C. K., Hsiao, T.-C., Lin, K.-Y., Lin, N.-H., Lin, W.-Y., et al. (2021). Analyzing the increasing importance of nitrate in Taiwan from long-term trend of measurements. *Atmospheric Environment*, *267*, 118749. https://doi.org/10.1016/j.atmosenv.2021.118749

Clarisse, L., Clerbaux, C., Dentener, F., Hurtmans, D., & Coheur, P.-F. (2009). Global ammonia distribution derived from infrared satellite observations. *Nature Geoscience*, *2*(7), 479–483. https://doi.org/10.1038/ngeo551

Clarisse, L., Coheur, P.-F., & Van Damme, M. (2022). Reanalyzed daily IASI ULB-LATMOS ammonia (NH_3) L2 product (version 3.1.0R) [Dataset]. IASI. https://iasi.aeris-data.fr/catalog/#masthead

Clarisse, L., Van Damme, M., Clerbaux, C., & Coheur, P. F. (2019). Tracking down global NH3 point sources with wind-adjusted superresolution. *Atmospheric Measurement Techniques*, *12*(10), 5457–5473. https://doi.org/10.5194/amt-12-5457-2019

Coheur, P.-F., Levelt, P., Clarisse, L., van Damme, M., Eskes, H., Veefkind, J. P., et al. (2021). Nitrosat, a satellite mission concept for mapping reactive nitrogen at the landscape scale. In *EGU general assembly*.

Cooper, M. J., Martin, R. V., Hammer, M. S., Levelt, P. F., Veefkind, P., Lamsal, L. N., et al. (2022). Global fine-scale changes in ambient NO_2 during COVID-19 lockdowns. *Nature*, *601*(7893), 380–387. https://doi.org/10.1038/s41586-021-04229-0

Cooper, M. J., Martin, R. V., Henze, D. K., & Jones, D. B. A. (2020). Effects of a priori profile shape assumptions on comparisons between satellite NO_2 columns and model simulations. *Atmospheric Chemistry and Physics*, *20*(12), 7231–7241. https://doi.org/10.5194/acp-20-7231-2020

Dang, R., Jacob, D. J., Shah, V., Eastham, S. D., Fritz, T. M., Mickley, L. J., et al. (2023). Background nitrogen dioxide (NO_2) over the United States and its implications for satellite observations and trends: Effects of nitrate photolysis, aircraft, and open fires. *Atmospheric Chemistry and Physics*, *23*(11), 6271–6284. https://doi.org/10.5194/acp-23-6271-2023

Dang, R., Jacob, D. J., Zhai, S., Pendergrass, D. C., Choi, J., Park, J., et al. (2023). The $PM_{2.5}$ nitrate observations that are collected in this study [Dataset]. Harvard Dataverse. https://doi.org/10.7910/DVN/FACICP

Duncan, B. N., Yoshida, Y., Olson, J. R., Sillman, S., Martin, R. V., Lamsal, L., et al. (2010). Application of OMI observations to a space-based indicator of NO_x and VOC controls on surface ozone formation. *Atmospheric Environment*, *44*(18), 2213–2223. https://doi.org/10.1016/j.atmosenv.2010.03.010

Eskes, H. J., Velthoven, P. F. J. V., Valks, P. J. M., & Kelder, H. M. (2003). Assimilation of GOME total-ozone satellite observations in a three-dimensional tracer-transport model. *Quarterly Journal of the Royal Meteorological Society*, *129*(590), 1663–1681. https://doi.org/10.1256/qj.02.14

Evangeliou, N., Balkanski, Y., Eckhardt, S., Cozic, A., Van Damme, M., Coheur, P. F., et al. (2021). 10-year satellite-constrained fluxes of ammonia improve performance of chemistry transport models. *Atmospheric Chemistry and Physics*, *21*(6), 4431–4451. https://doi.org/10.5194/acp-21-4431-2021

Fairlie, T. D., Jacob, D. J., Dibb, J. E., Alexander, B., Avery, M. A., van Donkelaar, A., & Zhang, L. (2010). Impact of mineral dust on nitrate, sulfate, and ozone in transpacific Asian pollution plumes. *Atmospheric Chemistry and Physics*, *10*(8), 3999–4012. https://doi.org/10.5194/acp-10-3999-2010

Farren, N. J., Davison, J., Rose, R. A., Wagner, R. L., & Carslaw, D. C. (2020). Underestimated ammonia emissions from road vehicles. *Environmental Science and Technology*, *54*(24), 15689–15697. https://doi.org/10.1021/acs.est.0c05839

Fountoukis, C., & Nenes, A. (2007). ISORROPIA II: A computationally efficient thermodynamic equilibrium model for K+-Ca2+-Mg2+-Nh(4)(+)-Na+-SO42--NO3--Cl--H2Oaerosols. *Atmospheric Chemistry and Physics*, *7*(17), 4639–4659. https://doi.org/10.5194/acp-7-4639-2007

Franchin, A., Fibiger, D. L., Goldberger, L., McDuffie, E. E., Moravek, A., Womack, C. C., et al. (2018). Airborne and ground-based observations of ammonium-nitrate-dominated aerosols in a shallow boundary layer during intense winter pollution episodes in northern Utah. *Atmospheric Chemistry and Physics*, *18*(23), 17259–17276. https://doi.org/10.5194/acp-18-17259-2018

Fu, X., Wang, T., Gao, J., Wang, P., Liu, Y. M., Wang, S. X., et al. (2020). Persistent heavy winter nitrate pollution driven by increased photochemical oxidants in northern China. *Environmental Science and Technology*, *54*(7), 3881–3889. https://doi.org/10.1021/acs.est.9b07248

Gulde, S., Kolm, M., Smith, D., Maurer, R., Bazalgette Courrèges-Lacoste, G., Sallusti, M., & Bagnasco, G. (2017). Sentinel 4: A geostationary imaging UVN spectrometer for air quality monitoring: Status of design, performance and development. In *International conference on space optics — ICSO 2014, SPIE*.

Guo, H., Otjes, R., Schlag, P., Kiendler-Scharr, A., Nenes, A., & Weber, R. J. (2018). Effectiveness of ammonia reduction on control of fine particle nitrate. *Atmospheric Chemistry and Physics*, *18*(16), 12241–12256. https://doi.org/10.5194/acp-18-12241-2018

Guo, H., Weber, R. J., & Nenes, A. (2017). High levels of ammonia do not raise fine particle pH sufficiently to yield nitrogen oxide-dominated sulfate production. *Scientific Reports*, *7*(1), 12109. https://doi.org/10.1038/s41598-017-11704-0

Guo, X., Wang, R., Pan, D., Zondlo, M. A., Clarisse, L., Van Damme, M., et al. (2021). Validation of IASI satellite ammonia observations at the pixel scale using in situ vertical profiles. *Journal of Geophysical Research: Atmospheres*, *126*(9), e2020JD033475. https://doi.org/10.1029/2020JD033475

Jin, X., Fiore, A., Boersma, K. F., Smedt, I. D., & Valin, L. (2020). Inferring changes in summertime surface ozone–NO_x–VOC chemistry over U.S. urban areas from two decades of satellite and ground-based observations. *Environmental Science and Technology*, *54*(11), 6518–6529. https://doi.org/10.1021/acs.est.9b07785

Kim, H., Zhang, Q., & Sun, Y. (2020). Measurement report: Characterization of severe spring haze episodes and influences of long-range transport in the Seoul metropolitan area in March 2019. *Atmospheric Chemistry and Physics*, *20*(19), 11527–11550. https://doi.org/10.5194/acp-20-11527-2020

Kim, J., Jeong, U., Ahn, M.-H., Kim, J. H., Park, R. J., Lee, H., et al., (2020). New era of air quality monitoring from space: Geostationary environment monitoring spectrometer (GEMS). *Bulletin America Meteorology Social*, *101*(1), E1–E22. https://doi.org/10.1175/BAMS-D-18-0013.1

Kim, Y., Kim, H., Kang, H., de Foy, B., & Zhang, Q. (2022). Impacts of secondary aerosol formation and long range transport on severe haze during the winter of 2017 in the Seoul metropolitan area. *Science of the Total Environment*, *804*, 149984. https://doi.org/10.1016/j.scitotenv.2021.149984

Kleinman, L. I. (1994). Low and high NO_x tropospheric photochemistry. *Journal of Geophysical Research*, *99*, 16831–16838.

Krotkov, N. A., Lamsal, L. N., Marchenko, S. V., Bucsela, E. J., Swartz, W. H., Joiner, J., & the OMI core team (2019). OMI/aura nitrogen dioxide (NO_2) total and tropospheric column 1- orbit L2 Swath 13 × 24 km V003 [Dataset]. GSFC. https://disc.gsfc.nasa.gov/datasets/OMNO2_003/summary

Lamsal, L. N., Krotkov, N. A., Vasilkov, A., Marchenko, S., Qin, W., Yang, E. S., et al. (2021). Ozone Monitoring Instrument (OMI) Aura nitrogen dioxide standard product version 4.0 with improved surface and cloud treatments. *Atmospheric Measurement Techniques*, *14*(1), 455–479. https://doi.org/10.5194/amt-14-455-2021

Leung, D. M., Shi, H., Zhao, B., Wang, J., Ding, E. M., Gu, Y., et al. (2020). Wintertime particulate matter decrease buffered by unfavorable chemical processes despite emissions reductions in China. *Geophysical Research Letters*, *47*(14), e2020GL087721. https://doi.org/10.1029/2020GL087721

Li, H., Cheng, J., Zhang, Q., Zheng, B., Zhang, Y., Zheng, G., & He, K. (2019). Rapid transition in winter aerosol composition in Beijing from 2014 to 2017: Response to clean air actions. *Atmospheric Chemistry and Physics*, *19*(17), 11485–11499. https://doi.org/10.5194/acp-19-11485-2019

Li, H., Zhang, Q., Zheng, B., Chen, C., Wu, N., Guo, H., et al. (2018). Nitrate-driven urban haze pollution during summertime over the North China Plain. *Atmospheric Chemistry and Physics*, *18*(8), 5293–5306. https://doi.org/10.5194/acp-18-5293-2018

Li, M., Zhang, Z., Yao, Q., Wang, T., Xie, M., Li, S., et al. (2021). Nonlinear responses of particulate nitrate to NO_x emission controls in the megalopolises of China. *Atmospheric Chemistry and Physics*, *21*(19), 15135–15152. https://doi.org/10.5194/acp-21-15135-2021

Lin, Y. C., Zhang, Y. L., Fan, M. Y., & Bao, M. (2020). Heterogeneous formation of particulate nitrate under ammonium-rich regimes during the high-$PM_{2.5}$ events in Nanjing, China, Atmos. *Chemical Physics*, *20*(6), 3999–4011. https://doi.org/10.5194/acp-20-3999-2020

Lu, M., Tang, X., Feng, Y., Wang, Z., Chen, X., Kong, L., et al. (2021). Nonlinear response of SIA to emission changes and chemical processes over eastern and central China during a heavy haze month. *Science of the Total Environment*, *788*, 147747. https://doi.org/10.1016/j.scitotenv.2021.147747

Luo, G., Yu, F., & Moch, J. M. (2020). Further improvement of wet process treatments in GEOS-Chem v12.6.0: Impact on global distributions of aerosols and aerosol precursors. *Geoscientific Model Development*, *13*(6), 2879–2903. https://doi.org/10.5194/gmd-13-2879-2020

Luo, G., Yu, F., & Schwab, J. (2019). Revised treatment of wet scavenging processes dramatically improves GEOS-Chem 12.0.0 simulations of surface nitric acid, nitrate, and ammonium over the United States, Geosci. *Model Dev*, *12*(8), 3439–3447. https://doi.org/10.5194/gmd-12-3439-2019

Luo, Z., Zhang, Y., Chen, W., Van Damme, M., Coheur, P. F., & Clarisse, L. (2022). Estimating global ammonia (NH_3) emissions based on IASI observations from 2008 to 2018. In *Atmos. Chem. Phys. Discuss., 2022* (pp. 1–22). https://doi.org/10.5194/acp-2022-216

Marais, E. A., Pandey, A. K., Van Damme, M., Clarisse, L., Coheur, P.-F., Shephard, M. W., et al. (2021). UK ammonia emissions estimated with satellite observations and GEOS-Chem. *Journal of Geophysical Research: Atmospheres*, *126*(18), e2021JD035237. https://doi.org/10.1029/2021JD035237

Martin, R. V., Chance, K., Jacob, D. J., Kurosu, T. P., Spurr, R. J. D., Bucsela, E., et al. (2002). An improved retrieval of tropospheric nitrogen dioxide from GOME. *Journal of Geophysical Research*, *107*(D20), ACH9-1–ACH9-21. https://doi.org/10.1029/2001JD001027

Martin, R. V., Fiore, A. M., & Van Donkelaar, A. (2004). Space-based diagnosis of surface ozone sensitivity to anthropogenic emissions. *Geophysical Research Letters*, *31*(6), L06120. https://doi.org/10.1029/2004GL019416

McDuffie, E. E., Smith, S. J., O'Rourke, P., Tibrewal, K., Venkataraman, C., Marais, E. A., et al. (2020). A global anthropogenic emission inventory of atmospheric pollutants from sector- and fuel-specific sources (1970–2017): An application of the Community Emissions Data System (CEDS). *Earth System Science Data*, *12*(4), 3413–3442. https://doi.org/10.5194/essd-12-3413-2020

Mebust, A. K., Russell, A. R., Hudman, R. C., Valin, L. C., & Cohen, R. C. (2011). Characterization of wildfire NOx emissions using MODIS fire radiative power and OMI tropospheric NO_2 columns. *Atmospheric Chemistry and Physics*, *11*(12), 5839–5851. https://doi.org/10.5194/acp-11-5839-2011

Nenes, A., Pandis, S. N., Kanakidou, M., Russell, A. G., Song, S., Vasilakos, P., & Weber, R. J. (2021). Aerosol acidity and liquid water content regulate the dry deposition of inorganic reactive nitrogen. *Atmospheric Chemistry and Physics*, *21*(8), 6023–6033. https://doi.org/10.5194/acp-21-6023-2021

Nenes, A., Pandis, S. N., Weber, R. J., & Russell, A. (2020). Aerosol pH and liquid water content determine when particulate matter is sensitive to ammonia and nitrate availability. *Atmospheric Chemistry and Physics*, *20*(5), 3249–3258. https://doi.org/10.5194/acp-20-3249-2020

Petetin, H., Sciare, J., Bressi, M., Gros, V., Rosso, A., Sanchez, O., et al. (2016). Assessing the ammonium nitrate formation regime in the Paris megacity and its representation in the CHIMERE model. *Atmospheric Chemistry and Physics*, *16*, 10419–10440. https://doi.org/10.5194/acp-16-10419-2016

Romer Present, P. S., Zare, A., & Cohen, R. C. (2020). The changing role of organic nitrates in the removal and transport of NOx. *Atmospheric Chemistry and Physics*, *20*(1), 267–279. https://doi.org/10.5194/acp-20-267-2020

Schmit, T. J., Li, Z., Gunshor, M. M., Iturbide-Iturbide, F., Yoe, J. G., McCorkel, J., & Heidinger, A. (2022). In *U.S. plans for geostationary hyperspectral infrared sounders, IGARSS 2022 - 2022 IEEE international geoscience and remote sensing symposium* (pp. 5411–5414).

Shah, V., Jacob, D. J., Dang, R., Lamsal, L. N., Strode, S. A., Steenrod, S. D., et al. (2023). Nitrogen oxides in the free troposphere: Implications for tropospheric oxidants and the interpretation of satellite NO_2 measurements. *Atmospheric Chemistry and Physics*, *23*(2), 1227–1257. https://doi.org/10.5194/acp-23-1227-2023

Shah, V., Jacob, D. J., Li, K., Silvern, R. F., Zhai, S. X., Liu, M. Y., et al. (2020). Effect of changing NO_x lifetime on the seasonality and long-term trends of satellite-observed tropospheric NO_2 columns over China. *Atmospheric Chemistry and Physics*, *20*(3), 1483–1495. https://doi.org/10.5194/acp-20-1483-2020

Shen, L., Jacob, D. J., Zhu, L., Zhang, Q., Zheng, B., Sulprizio, M. P., et al. (2019). The 2005–2016 trends of formaldehyde columns over China observed by satellites: Increasing anthropogenic emissions of volatile organic compounds and decreasing agricultural fire emissions. *Geophysical Research Letters*, *46*(8), 4468–4475. https://doi.org/10.1029/2019GL082172

Shephard, M. W., & Cady-Pereira, K. E. (2015). Cross-track Infrared Sounder (CrIS) satellite observations of tropospheric ammonia. *Atmospheric Measurement Techniques*, *8*(3), 1323–1336. https://doi.org/10.5194/amt-8-1323-2015

Sillman, S. (1995). The use of NO_y, H_2O_2, and HNO_3 as indicators for ozone-NO_x -hydrocarbon sensitivity in urban locations. *Journal of Geophysical Research*, *100*(D7), 14175–14188. https://doi.org/10.1029/94JD02953

Song, S., Nenes, A., Gao, M., Zhang, Y., Liu, P., Shao, J., et al. (2019). Thermodynamic modeling suggests declines in water uptake and acidity of inorganic aerosols in Beijing winter haze events during 2014/2015–2018/2019. *Environmental Science and Technology Letters*, *6*(12), 752–760. https://doi.org/10.1021/acs.estlett.9b00621

Stelson, A. W., & Seinfeld, J. H. (1982). Relative humidity and temperature dependence of the ammonium nitrate dissociation constant. *Atmospheric Environment*, *16*(5), 983–992. https://doi.org/10.1016/0004-6981(82)90184-6

Tian, M., Liu, Y., Yang, F., Zhang, L., Peng, C., Chen, Y., et al. (2019). Increasing importance of nitrate formation for heavy aerosol pollution in two megacities in Sichuan Basin, southwest China. *Environmental Pollution*, *250*, 898–905. https://doi.org/10.1016/j.envpol.2019.04.098

Van Damme, M., Clarisse, L., Franco, B., Sutton, M. A., Erisman, J. W., Kruit, R. W., et al. (2021). Global, regional and national trends of atmospheric ammonia derived from a decadal (2008–2018) satellite record. *Environmental Research Letters*, *16*(5), 055017. https://doi.org/10.1088/1748-9326/abd5e0

Van Damme, M., Clarisse, L., Heald, C. L., Hurtmans, D., Ngadi, Y., Clerbaux, C., et al. (2014). Global distributions, time series and error characterization of atmospheric ammonia (NH_3) from IASI satellite observations. *Atmospheric Chemistry and Physics*, *14*(6), 2905–2922. https://doi.org/10.5194/acp-14-2905-2014

van Geffen, J., Boersma, K. F., Eskesl, H., Sneep, M., ter Linden, M., Zara, M., & Veefkind, J. P. (2020). S5P TROPOMI NO_2 slant column retrieval: Method, stability, uncertainties and comparisons with OMI. *Atmospheric Measurement Techniques*, *13*(3), 1315–1335. https://doi.org/10.5194/amt-13-1315-2020

Vohra, K., Marais, E. A., Suckra, S., Kramer, L., Bloss, W. J., Sahu, R., et al. (2021). Long-term trends in air quality in major cities in the UK and India: A view from space. *Atmospheric Chemistry and Physics*, *21*(8), 6275–6296. https://doi.org/10.5194/acp-21-6275-2021

Wang, R., Pan, D., Guo, X., Sun, K., Clarisse, L., Van Damme, M., et al. (2023). Bridging the spatial gaps of the Ammonia Monitoring Network using satellite ammonia measurements. In *EGUsphere, 2023* (pp. 1–33). https://doi.org/10.5194/egusphere-2023-190

Wang, W., Liu, C., Clarisse, L., Van Damme, M., Coheur, P.-F., Xie, Y., et al. (2022). Ground-based measurements of atmospheric NH_3 by Fourier transform infrared spectrometry at Hefei and comparisons with IASI data. *Atmospheric Environment*, *287*, 119256. https://doi.org/10.1016/j.atmosenv.2022.119256

Wang, X., Jacob, D. J., Downs, W., Zhai, S., Zhu, L., Shah, V., et al. (2021). Global tropospheric halogen (Cl, Br, I) chemistry and its impact on oxidants. *Atmospheric Chemistry and Physics*, *21*(18), 13973–13996. https://doi.org/10.5194/acp-21-13973-2021

Wang, Y., Wen, Y., Zhang, S., Zheng, G., Zheng, H., Chang, X., et al. (2023). Vehicular ammonia emissions significantly contribute to urban $PM_{2.5}$ pollution in two Chinese megacities. *Environmental Science and Technology*, *57*(7), 2698–2705. https://doi.org/10.1021/acs.est.2c06198

Womack, C. C., McDuffie, E. E., Edwards, P. M., Bares, R., de Gouw, J. A., Docherty, K. S., et al. (2019). An odd oxygen framework for wintertime ammonium nitrate aerosol pollution in urban areas: NOx and VOC control as mitigation strategies. *Geophysical Research Letters*, *46*(9), 4971–4979. https://doi.org/10.1029/2019GL082028

Xu, Q., Wang, S., Jiang, J., Bhattarai, N., Li, X., Chang, X., et al. (2019). Nitrate dominates the chemical composition of $PM_{2.5}$ during haze event in Beijing, China. *Science of the Total Environment*, *689*, 1293–1303. https://doi.org/10.1016/j.scitotenv.2019.06.294

Xu, Z., Liu, M., Zhang, M., Song, Y., Wang, S., Zhang, L., et al. (2019). High efficiency of livestock ammonia emission controls in alleviating particulate nitrate during a severe winter haze episode in northern China. *Atmospheric Chemistry and Physics*, *19*(8), 5605–5613. https://doi.org/10.5194/acp-19-5605-2019

Zang, H., Zhao, Y., Huo, J., Zhao, Q., Fu, Q., Duan, Y., et al. (2022). High atmospheric oxidation capacity drives wintertime nitrate pollution in the eastern Yangtze River Delta of China. *Atmospheric Chemistry and Physics*, *22*(7), 4355–4374. https://doi.org/10.5194/acp-22-4355-2022

Zhai, S., Jacob, D. J., Pendergrass, D. C., Colombi, N. K., Shah, V., Yang, L. H., et al. (2023). Coarse particulate matter air quality in East Asia: Implications for fine particulate nitrate. *Atmospheric Chemistry and Physics*, *23*(7), 4271–4281. https://doi.org/10.5194/acp-23-4271-2023

Zhai, S., Jacob, D. J., Wang, X., Liu, Z., Wen, T., Shah, V., et al. (2021). Control of particulate nitrate air pollution in China. *Nature Geoscience*, *14*(6), 389–395. https://doi.org/10.1038/s41561-021-00726-z

Zhai, S., Jacob, D. J., Wang, X., Shen, L., Li, K., Zhang, Y., et al. (2019). Fine particulate matter ($PM_{2.5}$) trends in China, 2013–2018: Separating contributions from anthropogenic emissions and meteorology. *Atmospheric Chemistry and Physics*, *19*(16), 11031–11041. https://doi.org/10.5194/acp-19-11031-2019

Zhang, L., Chen, Y., Zhao, Y., Henze, D. K., Zhu, L., Song, Y., et al. (2018). Agricultural ammonia emissions in China: Reconciling bottom-up and top-down estimates. *Atmospheric Chemistry and Physics*, *18*(1), 339–355. https://doi.org/10.5194/acp-18-339-2018

Zheng, B., Tong, D., Li, M., Liu, F., Hong, C., Geng, G., et al. (2018). Trends in China's anthropogenic emissions since 2010 as the consequence of clean air actions. In *Atmos. Chem. Phys. Discuss., 2018* (pp. 1–27). https://doi.org/10.5194/acp-2018-374

Zhou, M., Nie, W., Qiao, L., Huang, D. D., Zhu, S., Lou, S., et al. (2022). Elevated formation of particulate nitrate from N_2O_5 hydrolysis in the Yangtze River Delta region from 2011 to 2019. *Geophysical Research Letters*, *49*(9), e2021GL097393. https://doi.org/10.1029/2021GL097393

Zhu, L., Jacob, D. J., Keutsch, F. N., Mickley, L. J., Scheffe, R., Strum, M., et al. (2017). Formaldehyde (HCHO) as a hazardous air pollutant: Mapping surface air concentrations from satellite and inferring cancer risks in the United States. *Environmental Science and Technology*, *51*(10), 5650–5657. https://doi.org/10.1021/acs.est.7b01356

Zhu, L., Jacob, D. J., Mickley, L. J., Marais, E. A., Cohan, D. S., Yoshida, Y., et al. (2014). Anthropogenic emissions of highly reactive volatile organic compounds in eastern Texas inferred from oversampling of satellite (OMI) measurements of HCHO columns. *Environmental Research Letters*, *9*(11), 114004. https://doi.org/10.1088/1748-9326/9/11/114004

References From the Supporting Information

Chow, W. S., Liao, K., Huang, X. H. H., Leung, K. F., Lau, A. K. H., & Yu, J. Z. (2022). Measurement report: The 10-year trend of $PM_{2.5}$ major components and source tracers from 2008 to 2017 in an urban site of Hong Kong, China. *Atmospheric Chemistry and Physics*, *22*(17), 11557–11577. https://doi.org/10.5194/acp-22-11557-2022

Liu, Y., Wang, J., Zhao, X., Wang, J., Wang, X., Hou, L., et al. (2020). Characteristics, secondary formation and regional contributions of $PM_{2.5}$ pollution in Jinan during winter. *Atmosphere*, *11*, 273.

Sun, J., Qin, M., Xie, X., Fu, W., Qin, Y., Sheng, L., et al. (2022). Seasonal modeling analysis of nitrate formation pathways in Yangtze River Delta region, China. *Atmospheric Chemistry and Physics*, *22*(18), 12629–12646. https://doi.org/10.5194/acp-22-12629-2022

Wang, X., Wei, W., Cheng, S., Zhang, H., & Yao, S. (2019). Source estimation of SO_4^{2-} and NO_3^- based on monitoring-modeling approach during winter and summer seasons in Beijing and Tangshan, China. *Atmospheric Environment*, *214*, 116849. https://doi.org/10.1016/j.atmosenv.2019.116849

Zhang, Q., Zheng, Y., Tong, D., Shao, M., Wang, S., Zhang, Y., et al. (2019). Drivers of improved $PM_{2.5}$ air quality in China from 2013 to 2017. *Proceedings of the National Academy of Sciences*, *116*(49), 24463–24469. https://doi.org/10.1073/pnas.1907956116

Zhao, L., Wang, L., Tan, J., Duan, J., Ma, X., Zhang, C., et al. (2019). Changes of chemical composition and source apportionment of PM2.5 during 2013–2017 in urban Handan, China. *Atmospheric Environment*, *206*, 119–131. https://doi.org/10.1016/j.atmosenv.2019.02.034